Earth and Planetary Science Letters 394 (2014) 111–123

Contents lists available at ScienceDirect

Earth and Planetary Science Letters

www.elsevier.com/locate/epsl

Insights into the dynamics and evolution of the 2010 Eyjafjallajökull summit eruption (Iceland) provided by volcanic ash textures

R. Cioni [a,*], M. Pistolesi [a,b], A. Bertagnini [c], C. Bonadonna [d], A. Hoskuldsson [e], B. Scateni [b]

[a] Department of Earth Sciences, University of Florence, Italy
[b] Department of Earth Sciences, University of Pisa, Italy
[c] Istituto Nazionale di Geofisica e Vulcanologia, Sezione di Pisa, Italy
[d] Section of Earth and Environmental Sciences, University of Geneva, Switzerland
[e] NordVulk, Institute of Earth Sciences, University of Iceland, Reykjavik, Iceland

ARTICLE INFO

Article history:
Received 31 May 2013
Received in revised form 23 January 2014
Accepted 26 February 2014
Available online 1 April 2014
Editor: T. Elliott

Keywords:
explosive volcanism
volcanic ash
ash morphology
hydromagmatic eruptions
Eyjafjallajökull

ABSTRACT

The April–May 2010 eruption of the Eyjafjallajökull volcano (Iceland) represents an example of explosive activity dominated by prolonged, low- to mid-intensity emission of ash, as it was characterized by a continuous injection of tephra into the atmosphere that affected various economic sectors in Iceland and caused a world-wide interruption of air traffic. This eruption has become a benchmark for the understanding of the processes that govern the dynamics of ash-dominated eruptions, also representing a unique opportunity for direct ash particle investigation.

In this paper, selected ash samples from all phases of the eruption were studied in order to characterize: 1) the morphology, composition and texture of ash fragments; 2) the variability of the products of each phase of the eruption; 3) the progressive changes of these features with time. The large morphological and textural variability of the ash fragments throughout the eruption is unrelated to any important compositional change, and it reflects changes in eruption dynamics and in the mechanisms of magma fragmentation. Textural and morphological features of juveniles suggest that primary magma degassing dominated and modulated the dynamics of the entire eruption, while hydromagmatic fragmentation was particularly effective only in the very initial phase. As a consequence, the large production of fine-grained ash cannot be attributed to processes of magma–water interaction, and mechanisms of brittle to ductile fragmentation related to magma degassing or ash recycling must be invoked. The study demonstrates how the textural and morphological analysis of ash fragments can give important hints to the understanding of the eruption dynamics of complex, long lasting eruptions.

© 2014 Elsevier B.V. All rights reserved.

1. Introduction

The products of mid- to low-intensity eruptions (e.g. subPlinian, violent Strombolian, Vulcanian) are characterized by variability of the juvenile fraction, in response to the complex dynamics of magma degassing and fragmentation. These eruptions are often characterized or accompanied by prolonged phases of dominant ash emission (Sparks et al., 1997; Cioni et al., 2008), and the study of ash textures and morphology can be especially effective for defining the processes which dominate magma ascent, degassing and fragmentation. These are recorded in the textural features of the ash, mainly as variations in vesicle shape, size and abundance, and crystal content and composition of the groundmass (Nakada and Motomura, 1999; Hammer et al., 2000; Cioni et al., 2003; Wright et al., 2012). The variability of these parameters during eruptions has been successfully used to constrain eruption dynamics (Taddeucci et al., 2004; Lautze and Houghton, 2005; D'Oriano et al., 2011). Morphologic features of ash particles have been also widely used to infer genetic processes of pyroclastic deposits.

The predominance of fine-grained material (ash) in the products of explosive eruptions has been often related to processes of magma–water interaction (Self and Sparks, 1978; Heiken and Wohletz, 1985), and some specific morphologic features have been considered sufficient to indicate the dominance of hydromagmatic fragmentation processes (Heiken and Wohletz, 1985; Dellino and La Volpe, 1996). Despite these ideas, there is increasing evidence of efficient production of volcanic ash due to primary (magmatic) explosive fragmentation, driven by massive vesiculation of a viscous melt (Zimanowski et al., 2003; Rose and Durant, 2009).

Wide research effort has been dedicated in the last two years to the study of the March–May 2010 eruption of Eyjafjallajökull

* Corresponding author.

http://dx.doi.org/10.1016/j.epsl.2014.02.051
0012-821X/© 2014 Elsevier B.V. All rights reserved.

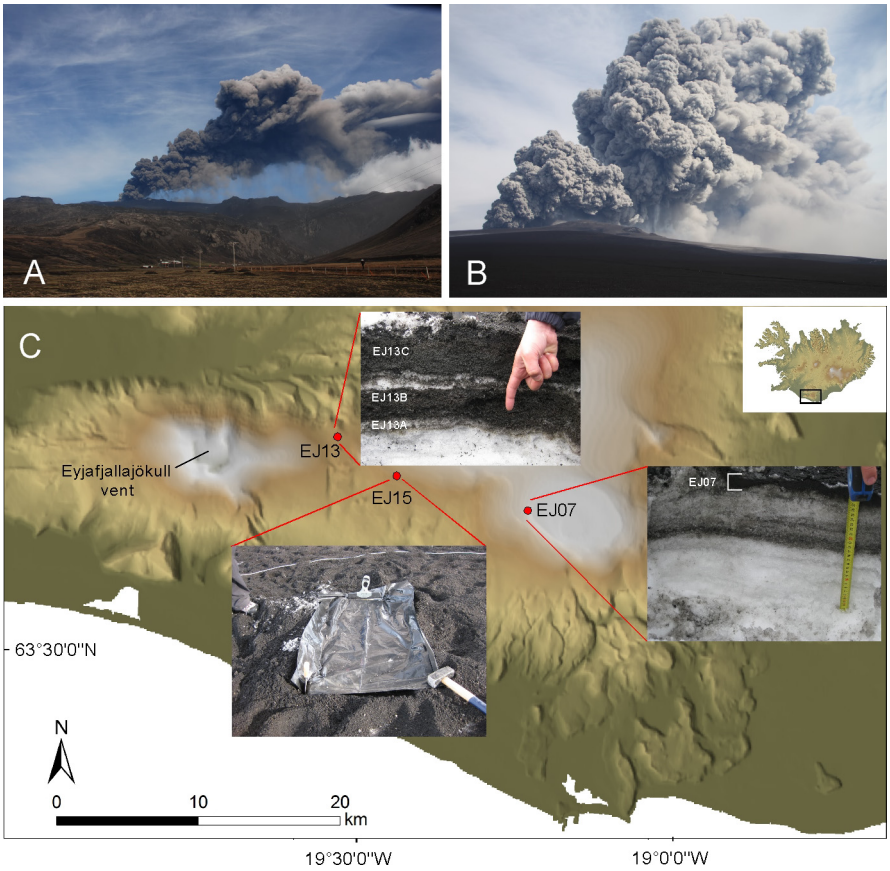

Fig. 1. Ash plume on May 4 2010 as seen from the South (A); activity on May 7 from the western rim of the crater (B); Three main sampling sites located at 4.5 (EJ13), 9 (EJ15) and 20 km (EJ07) from the vent, respectively. Samples at sites EJ13 and EJ07 were collected in pristine sections packed in the snow. Sample EJ15 was collected over black plastic bags during direct fallout from the plume (C).

(Iceland) (e.g., Bonadonna et al., 2011; Kaminski et al., 2011; Taddeucci et al., 2011; Bagnato et al., 2012; Borisova et al., 2012; Dellino et al., 2012; Gislason et al., 2011; Gudmundsson et al., 2012). This eruption represents a unique opportunity for ash particle investigation, as its nearly continuous injection of fine-grained ash into the atmosphere was observed in detail, and particle sedimentation sampled in near-real time. Only few studies have been conducted in detail to investigate the actual fragmentation process (Dellino et al., 2012; Gudmundsson et al., 2012). Based on classical morphological observations on the ash fragments, these works concluded that magma–ice/water interaction was particularly effective during the first, highly explosive phase of the eruption (first two weeks), while in the rest of the eruption the contribution of external water to the dynamics was not significant. No other data have been collected in order to document the process of ash production during the entire eruption, and to relate the differences in the erupted material with the variations in the eruptive dynamics. In this paper, selected samples from the various phases of the eruption are studied to characterize ash in terms of morphology, composition and texture. The variability of the products from each phase is discussed in detail, as well as the progressive changes of these features with time. Finally, we use our results to discuss magma fragmentation processes (magmatic versus hydromagmatic), and changes in eruption and magma dynamics during the different phases of the eruption.

2. Chronology of the 2010 eruption

The 14 April–21 May 2010 eruption of Eyjafjallajökull was characterized by a nearly continuous injection of tephra into the atmosphere, up to 9 km above sea level (Fig. 1A and B). Ash was mainly dispersed towards the east and south-east (Fig. 1C) reaching as far as the southern parts of Europe and causing significant damage to vegetation and various economic sectors in Iceland, combined with a global disruption to air traffic (Miller, 2011; O'Regan, 2011; Gudmundsson et al., 2012).

The explosive activity was preceded by a mildly Na-alkaline, basaltic fissure eruption on the east flank (Fimmvörðuháls) of the volcano, with activity characterized by up to 150 m-high lava fountains and lava emplacement (20 March–12 April). Activity recommenced inside the summit caldera in the early morning of 14 April. The summit eruption consisted of three phases (Höskuldsson, 2011; Gudmundsson et al., 2012); Phase I (14–18 April) can be subdivided in two further stages. A first opening stage (first 3–4 hours) started when the eruption melted its way through the ice-filled summit caldera. Steam-dominated and ash-poor plumes characterized this stage. Meltwater started to generate jökulhlaups (floods) from the ice cap around 7 am (local time). The eruption plume was observed earlier in the morning on 14 April. The first aerial survey revealed a series of vents aligned along a 2 km-long, north-south-oriented fissure (Magnússon et al., 2012).

The second stage of Phase I started around 6:30 pm of 14 April, when a dark ash-laden plume emerged from the summit vents, and lasted until 18 April. From 15 April, activity concentrated in the summit area and remained within the cauldron until the end of the eruption (Gudmundsson et al., 2012). Pulsating explosions (hydromagmatic-like), occurring on the interval of seconds to tens of seconds, characterized this second stage of Phase I. Each pulse was formed by a steady stream of explosive events which supported a 5–7 km-high ash-rich eruption plume (Höskuldsson, 2011), with large magma or ice blocks trailing cock-tail jets of

black material and pyroclastic surges limited to the caldera area. Due to the unusually stable jet stream present at the time, the ash cloud reached mainland Europe, forcing the closure of airspace over a large part of Northern Europe. The most voluminous ash-producing pulses took place in the afternoons of 14, 16 and from noon on the 17 to early morning of the 18 of April. The average volume flow rate (Q) for the first 72 hours of the eruption was estimated at about 200–400 $m^3\,s^{-1}$ Dense Rock Equivalent (DRE) (Gudmundsson et al., 2012).

The intensity of the eruption drastically dropped on 19 April (start of Phase II), followed by the onset of a lava flow which lasted until 4 of May. This was accompanied by a semi-continuous discharge of meltwater and steaming from the northern edge of the ice cauldron due to the lava flowing underneath the Gígjökull glacier, with no signs of major water accumulation within the summit cauldron. This phase was characterized by small eruptive plumes (2–3 km above the vent) and an average $Q < 35$ $m^3\,s^{-1}$ (Gudmundsson et al., 2012). Erupted material continued to accumulate within the summit area leading to the build-up of a tephra rampart on top of the northern side of the ice cauldron. The height of the crater cone was 150 ± 20 m on 26 April (Thorkelsson, 2012).

A new phase of explosive activity started on 5 May (Phase III) with renewed production of nearly continuous ash-rich columns rising to heights in excess of 5 km (up to 10 km). Activity alternated short periods of low magma discharge (15–30 $m^3\,s^{-1}$) with prolonged periods of high discharge (100–350 $m^3\,s^{-1}$), similar to those observed during the main stage of Phase I (Bonadonna et al., 2011; Höskuldsson, 2011; Gudmundsson et al., 2012). The onset of this phase was also marked by the concurrent cessation of the lava emission. Ash puffs were ejected every about 20 seconds at an average speed of 45 m/s (range of 20–150 m/s; Ripepe et al., 2013). A final, waning tail (Phase IV) closed the eruption around 22 May 2010 (Gudmundsson et al., 2012).

The total bulk volume of tephra emitted during the 39 days of activity has been estimated at $270 \pm 70 \times 10^6$ m^3 (equivalent to 0.18 ± 0.05 km^3 DRE), of which $140 \pm 20 \times 10^6$ m^3 fell on Iceland (Gudmundsson et al., 2012). About 70% of material was produced during the Phase I; Bonadonna et al. (2011) estimated that at least 30% of the ash erupted during Phase III was finer than 63 μm.

3. Tephra sampling and general stratigraphy

An extensive tephra sampling was carried out between 2 and 56 km from the vent, east and southeast of the volcano (Fig. 1C). Five ash samples representative of the main phases of the eruption were selected and used for the morphology and textural studies. Sampling representativeness is guaranteed by the general fine-grained nature of the erupted material (Wright et al., 2012).

Tephra emplaced during Phases I and II were collected from the fall deposits interbedded with the snow in sections EJ13 and EJ07. Section EJ13 (Fig. 1C) is located 4.5 km east of the crater and is an approximately 20 cm-thick sequence of tephra beds separated by snow. Three samples were collected at this site: the basal sample (EJ13A) is from a 2 cm-thick, coarse ash deposit. The overlying horizon, from which sample EJ13B was collected, is a 5 cm-thick layer of coarse-grained ash with scattered vesicular juvenile lapilli. A thin, discontinuous, snow layer separates EJ13B from the overlying upper tephra layer (EJ13C) which is represented by a fine-grained, 10 cm-thick, faintly stratified ash bed. The EJ13 section is very similar to that described by Thordarson (2010) and photographed a few days after the onset of the summit eruption. Based on this stratigraphy, sample EJ13A was attributed to the first hours of the eruption (opening stage of Phase I, 14 April), and EJ13B and EJ13C to Phase I (14–17 April), during which most of the tephra sequence was deposited.

Section EJ07, approximately 20 km east from the vent (Fig. 1C), is represented by a basal, 10 cm-thick layer of fine-grained tephra packed in the snow, covered by a discrete ash layer (sample EJ07; Fig. 1C); this topmost ash deposit was attributed to the tephra accumulated during the entire Phase II (19 April–4 May).

Tephra of Phase III was collected approximately 9 km east of the crater as it fell from the plume on 5 May (sample EJ15; Fig. 1C). Falling tephra was mainly aggregated ash of variable sizes, which mostly disaggregated on impact with the ground (see Bonadonna et al., 2011 for more details on tephra fallout and sampling during Phase III).

The first observation of the tephra deposits in the field revealed that different types of juvenile clasts coexisted within each level, and that the relative abundance of these different clasts also varied with the stratigraphic height. Juvenile fragments (always accounting for more than 85 wt% of the samples) varied from dense, poorly-vesicular obsidian clasts up to highly-vesicular, elongated pumice, to scoria fragments. Fragments of altered lavas and scoriae mainly formed the lithic fraction.

4. Data

4.1. Grain-size

Grain-size analyses show a bimodal distribution for all the five samples studied, with main modes ranging from -1ϕ to 2ϕ and from 4ϕ to 5ϕ (Fig. 2). Bonadonna et al. (2011) suggested this bimodality is related to processes of early ash aggregation in the plume, also confirmed by the observations of Taddeucci et al. (2011). Since not all samples were collected at the same distance from vent, grain-size cannot be directly related to variations in eruptive dynamics. The tephra sequence collected at the EJ13 site (Fig. 1C), which represents the activity of 14–17 April, is characterized at the base (EJ13A and B) by a uniform grain-size ($Md_\Phi = -0.8$), drastically decreasing to the top (EJ13C; $Md_\Phi = 2.5$), and consistent with a progressive decrease in the intensity of the eruption during Phase I and with the observed southward shift of the dispersal axis of the plume of the 17 April activity (Gudmundsson et al., 2012).

4.2. Juvenile component

4.2.1. Types of juvenile fragments

The overall morphological and textural features of the juvenile material, and the relative proportions of the different clast types were defined in the coarse ash fraction (0ϕ). The choice of this fraction represents a good compromise between the representativeness of this material with respect to the deposit, and the possibility to recognize in its textural features the pre-fragmentation state of the magma. Analysis of clasts finer than 4ϕ (representative of the fine ash fraction) was also performed in order to detect the homogeneity of the juvenile material in terms of morphology and surface features. The results of the study of the two ash fractions evidence the existence of at least four main categories of juvenile clasts, that were distinguished on the basis of morphology, dimensional ratios, features and shape of the external surfaces, amount and dimensional ratios of vesicles (Figs. 3 to 5).

Spongy, finely vesicular clasts (SFV) are characterized by very irregular external surfaces, due to the presence of broken, thin (<10 μm) bubble septa. Clast vesicularity is generally high (mean value 58 vol.%, range 35–73 vol.%); vesicles are roughly equidimensional and homogeneously distributed. Most of the vesicles are smaller than 100 μm. Vesicle shape varies from equant to subequant.

Coarsely vesicular clasts (CV) have slightly irregular, planar to curviplanar external surfaces, with few protruding septa or fluidal

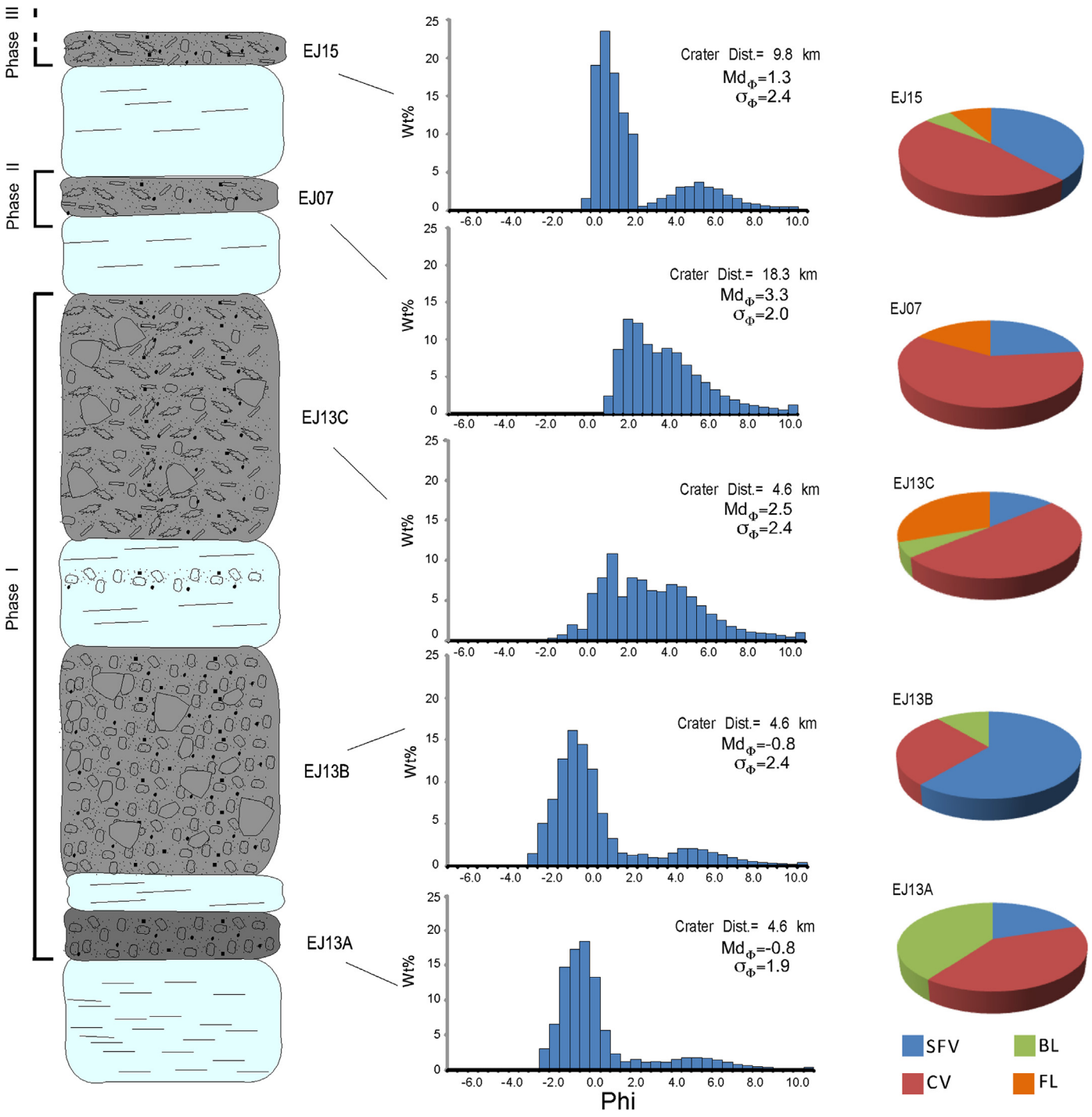

Fig. 2. Reconstructed stratigraphic sequence of the eruption from April 14 to May 5, 2010. Grain-size histograms and granulometric parameters are reported on the right. Proportions of different types of juvenile material within each sample are shown on the right (SFV = spongy finely vesicular, BL = blocky, CV = coarse vesicular, FL = fluidal).

sectors, and equant to moderately elongate shapes. Morphology is determined by the intersection of the external surface with coarse vesicles (>100 μm). Clast vesicularity varies between 27–70 vol.% and highly vesicular clasts (60–70 vol.% vesicles) predominate. Vesicles are spherical to irregular, with a large dimensional range.

Blocky clasts (BL) have equant to sub-equant, roughly prismatic shapes, showing planar to curviplanar, to slightly irregular, external surfaces that rarely intersect vesicles. Curviplanar surfaces possibly result from rupture of very coarse bubbles or not vesicular glass. Clasts are generally incipiently to moderately vesicular (12–40 vol.%), with a modal value around 30 vol.%. Black, obsidian-like glassy clasts characterized by smooth external surfaces are present at the base of the succession. Vesicles are generally spherical, with a wide dimensional range. Elongate tubular, coalescing vesicles showing a preferred orientation are also present in some BL clasts. On average, these are characterized by the highest values of vesicularity for this category.

Fluidal clasts (FL) are sub-equant to elongate (rod-like). The general shape is moderately to very irregular, with a smooth-skinned surface; external surfaces cut only few bubbles. Clast vesicularity varies in the same range of SFV and CV clasts (34–70 vol.%), with a mode at approximately 55 vol.%. Vesicles

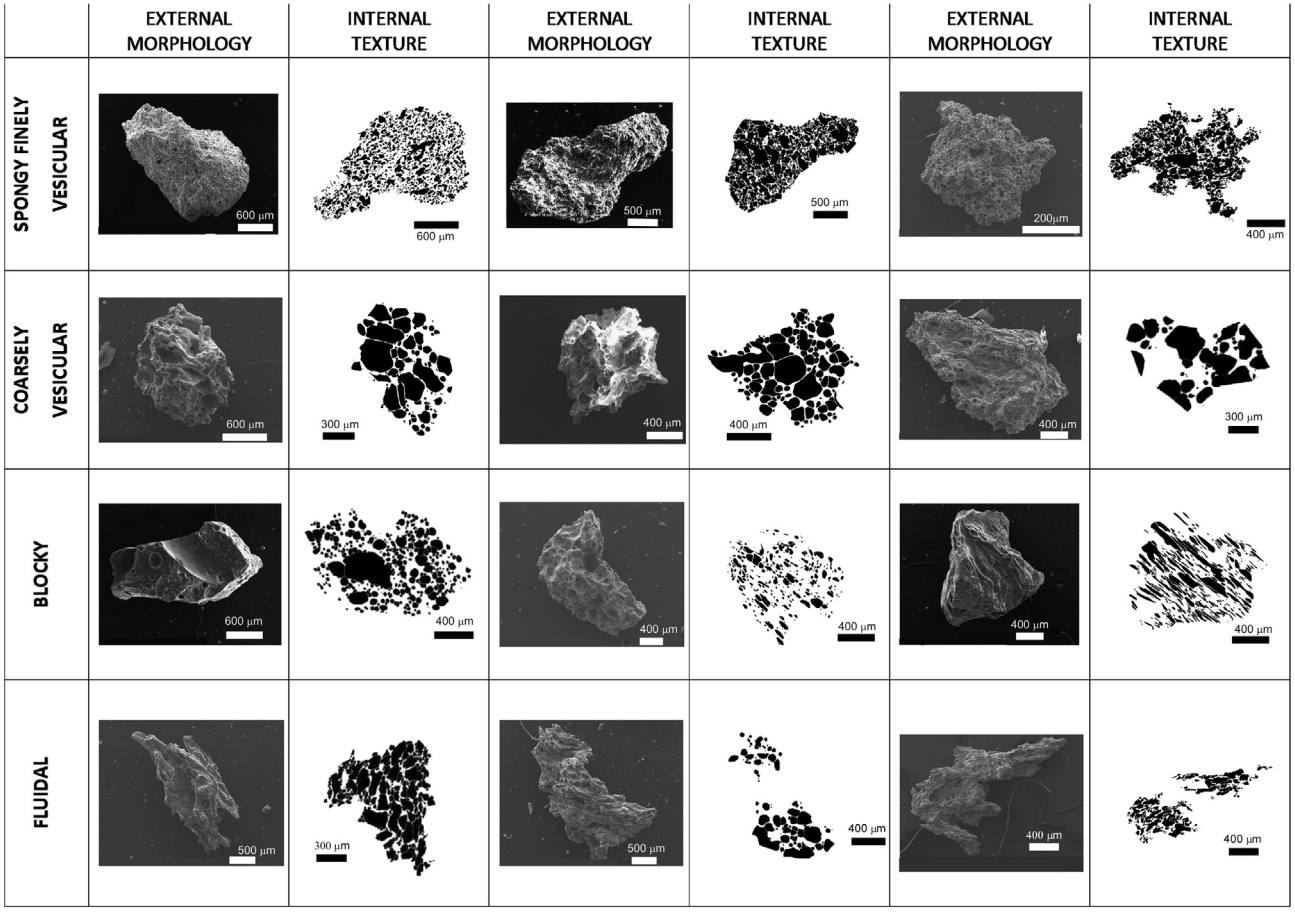

Fig. 3. SEM backscattered images of the four different types of juvenile material. Each clast is also characterized with the binary image of its internal vesicularity.

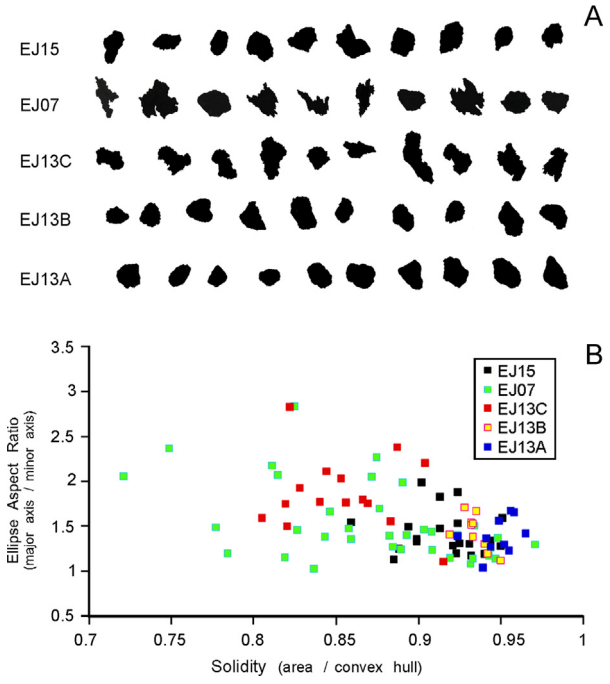

Fig. 4. (A) External morphologies of juvenile clasts for the different samples (i.e. different phases of the eruption). (B) Solidity vs ellipse aspect ratio during different phases of the eruption.

have a wide dimensional range, with the coexistence of large, irregular, contorted, elongated vesicles, and small-sized, nearly spherical ones. The smooth-skinned surfaces visible on these clasts possibly represent the inner surface of a population of very large, irregular bubbles (or of a complex network of interconnected bubbles), disrupted at fragmentation.

Open cracks, typical of hydromagmatic clasts (Heiken and Wohletz, 1985), were not observed in these fragments, but these do occasionally exhibit jigsaw-like fractures with very thin (submicrometer) openings. External surfaces of the clasts do not generally show coatings; if present, coatings are very fine-grained, formed by micrometer-sized ash. Vesicle filling is common, in particular in SFV and CV clasts. Secondary minerals are present on the external surfaces of some clasts throughout the whole sequence. They are mainly represented by diffuse, sub-micrometer-sized, salt encrustations, and by minor acicular to needle-like crystals (sulphates and possibly Na–Ca–K silicates), micrometer-sized cubic minerals (chlorides), and micrometer-sized globular masses composed of oxides and/or hydroxides. Combining information from direct measurements of surface composition and speciation modeling, Gislason et al. (2011) suggested the presence of a largely varied assemblage of sulphates, chlorides, fluorides, borates and phosphates in these salts encrustations. Bonadonna et al. (2011) described abundant ash coatings on particles directly collected on adhesive paper while falling. These ash coatings were however efficiently removed during the minute-long mechanical sieving, suggesting that syn-eruptive ash aggregation was mainly controlled by electrostatic forces, and that the formation of the secondary minerals was not sufficiently pervasive to cement the ash coatings.

4.2.2. Clast type abundance along the eruption sequence

The juvenile component ejected during the different phases of the eruption shows a large morphological and textural variability

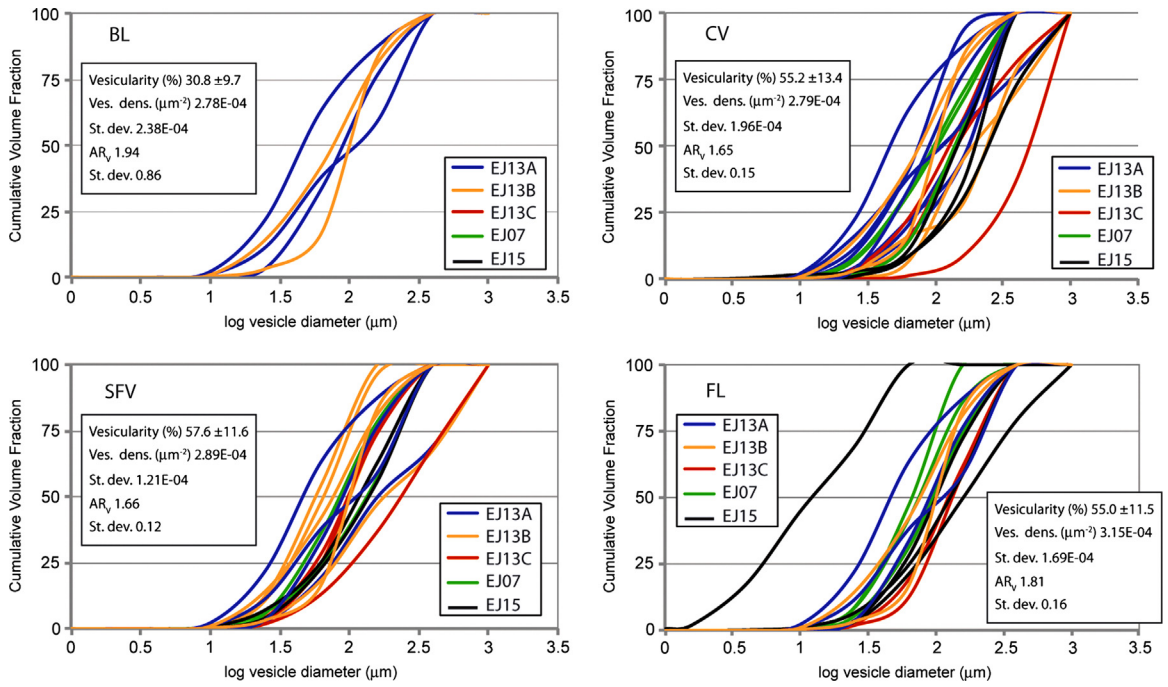

Fig. 5. Distribution of the vesicle size vs cumulative volume fractions for the different clast types. Different colors indicate different samples. Vesicularity, vesicle density and vesicle aspect ratio AR_V (and related standard deviations) are also reported in the insets for each clast type. (For interpretation of the colours in this figure, the reader is referred to the web version of this article.)

also at the scale of the single eruptive phase (Fig. 2). Noteworthy is the abundance of BL clasts in the products of the beginning of the first phase of the eruption (opening stage of Phase I; sample EJ13A) and the progressive decrease of this type of clasts up to their nearly complete disappearance at the end of this first phase (i.e., sample EJ13C; Fig. 3). Conversely, FL clasts first appear and are most abundant by the end of Phase I, and progressively decrease until Phase III. CV and SFV clasts are present in various proportions in all samples. However, the percentage of CV clasts is relatively constant, whereas SFV dominate in the products of the most intense episode of Phase I (EJ13B). SFV clasts are also abundant in the products of Phase III. All these observations can be summarized in the main following points:

i. the most diagnostic clast types for eruptive dynamics are BL and FL, as they are not always present, with BL being most abundant and FL being absent in the first stage of Phase I.
ii. low-vesicularity, BL clasts are abundant only at the onset of the eruption, together with coarsely vesicular clasts (CV);
iii. fluidal, highly vesicular clasts (FL) appear and are most abundant by the end of Phase I and during Phase II;
iv. coarsely vesicular clasts (CV) and highly vesicular clasts (SFV) are the only two components that are always present in all samples;
v. SFV clasts, which record the most vesicular portions of the magma, are particularly abundant in the tephra deposited by the most intense phases of the eruption (Phase I, Phase III).

4.2.3. Shape parameters

Projected outlines of the juvenile clasts depict a clear morphological variability along the eruption sequence, with jagged, irregular, elongated clasts being predominant by the end of Phase I to the end of Phase II (samples EJ13C and EJ07; Fig. 4A), and more compact, circular shapes mainly present between the clasts of the first part of Phase I. Among all the different morphological parameters calculated for the clasts, the solidity and ellipse aspect ratio values (see Methods in Electronic Supplementary Materials, ESM) clearly point out some of the difference in clast morphology observed between the products of the different phases of the eruption (Fig. 4B). The relative abundance of FL and BL clasts appears to control the trend of the morphological features, with the clasts from the first phase of the eruption (sample EJ13A) being mainly characterized by high values of convexity, solidity and circularity (Fig. 4B). Conversely, the abundance of both CV and FL clasts in the ash erupted at the end of Phase I (EJ13C) results in a large spread of all the shape parameters, due to the irregularity of the external surface of these clast types. Phase II clasts (EJ07) show the largest spread of all the shape parameters, reflecting the very large variability of clast types that characterizes this sample (Fig. 2).

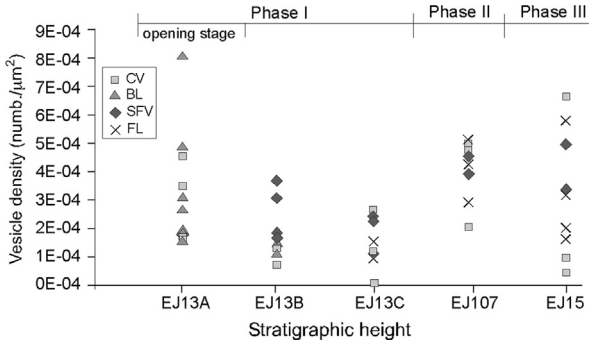

Fig. 6. Vesicle density (number/μm^2) for the different clast types as a function of the stratigraphic height.

4.2.4. Vesicle size, shape and number density

The different clast types have average vesicularity values around 55 vol.% except for the BL clasts, which present a lower vesicle content (around 30 vol.%; Fig. 5). Vesicularity of each clast type does not vary along the eruption; conversely, a change is observed for the vesicle number density per unit area N_a, characterized by a continuous decrease during Phase I (samples EJ13A to C), followed by an increase in the transition to Phase II (sample EJ07) and by a very large range in Phase III (sample EJ15; Fig. 6). 3D vesicle size

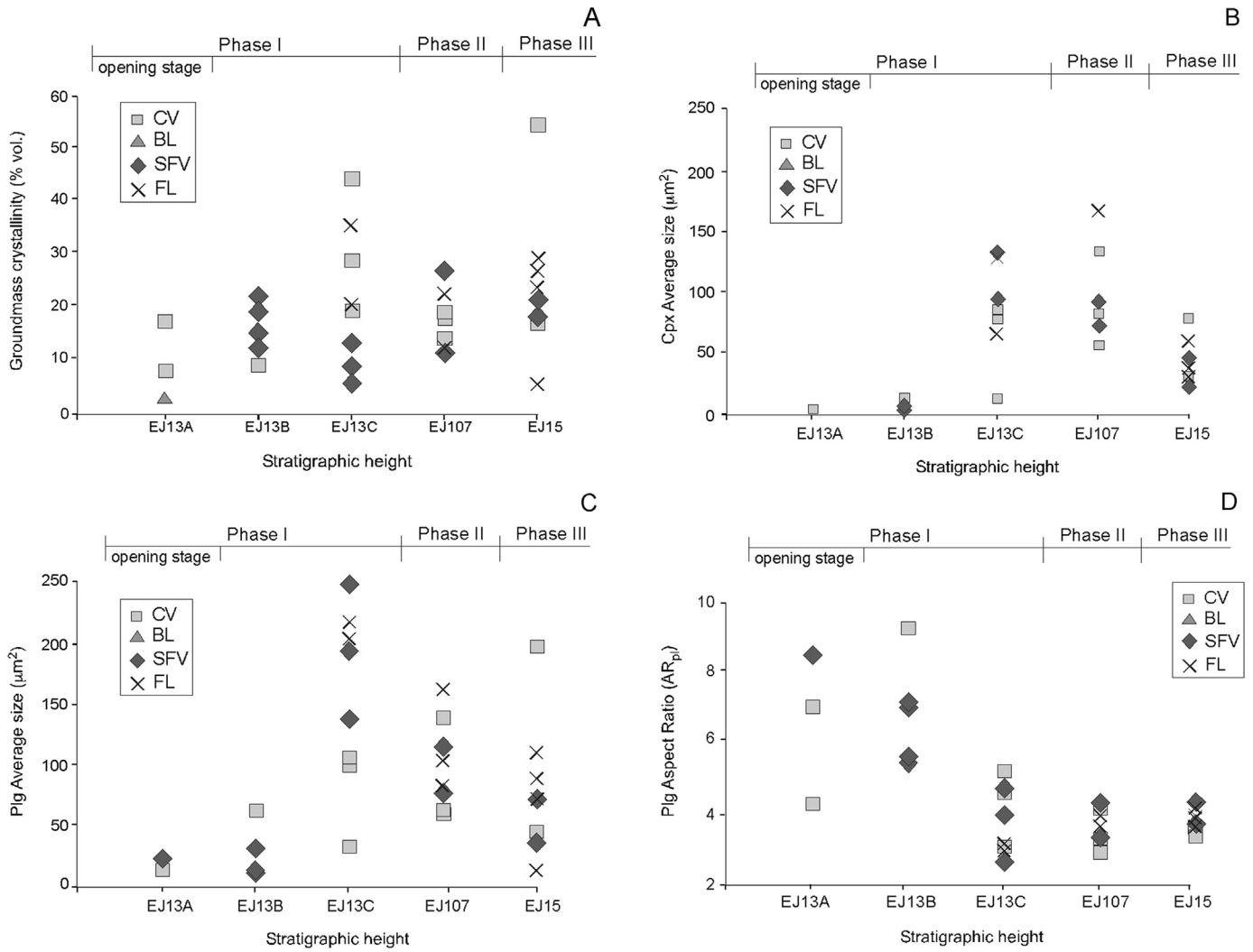

Fig. 7. (A) Distribution of the total groundmass crystallinity for the different clast types as a function of stratigraphic height. The different types of juvenile clasts are also characterized along the eruption sequence by (B) clinopyroxene and plagioclase (C) average size (μm^2) and (D) plagioclase aspect ratio (AR_{pl}).

distribution (calculated correcting 2D data according to the method by Klug and Cashman, 1994) of BL and SFV clasts is generally unimodal (Fig. 5), with a median diameter between 50 and 100 μm. The wider range of vesicle sizes shown by CV and FL clasts, and the shape of the cumulative curves reflect in some cases the presence of various populations of vesicles, possibly related to multiple stages of nucleation and growth, with a median vesicle diameter more variable than that of SFV. Aspect ratio of the vesicles (AR_v: ratio between the major and minor axes of the approximating ellipse) is high and largely variable for BL clasts (mean = 1.95, stdev = 0.87), reflecting the coexistence of BL clasts with tubular and spherical vesicles. AR_v is also higher for FL clasts (mean = 1.81, stdev = 0.17) than for CV and SFV clasts (mean = 1.65, stdev = 0.15, and mean = 1.66, stdev = 0.12, respectively).

4.2.5. Groundmass crystallinity

The range of total groundmass crystallinity is quite similar for CV, SFV and FL clasts, with the majority of them having average crystal content between 3 and 35 vol.% (Fig. 7A). The median value of the three clast types progressively increases from SFV, to CV, to FL, respectively passing from 14, to 17.6, to 22.8 vol.%. Two values larger than 40 vol.% are present in the CV clasts. BL clasts are present both as abundant, nearly microlite-free, glassy clasts in the deposits of the opening phase of the eruption (sample EJ13A), and as rare fragments from the rest of the sequence characterized by a glass-bearing groundmass carrying abundant, tiny microlites. Due to the very small amount of this second type of BL clasts in the sequence (samples EJ13B to EJ15, Fig. 2), only some microlite-poor BL clasts from the basal sample (EJ13A) were analyzed. Basing on this premise, an evolution of the groundmass crystal population can be observed from the base to the top of the sequence. A small but nearly continuous increase in crystallinity is observed in fact along the eruptive sequence (Fig. 7A), passing from the poorly crystallized clasts of the onset of Phase I (EJ13A; ≈7 vol.% on average), to the more crystallized samples of the end of Phase I (EJ13C; ≈22 vol.%), up to Phase III (EJ15; ≈25 vol.%). Variable proportions of plagioclase and subordinate clinopyroxene, and minor oxides form the mineral assemblage of the groundmass. Size of clinopyroxene microlites follows a similar trend, with a maximum shifted to Phase II (Fig. 7B). On average, the largest microlites are associated with the end of Phase I and Phase II. Average dimensions of plagioclase microlites show a general increase from the base of the sequence to the end of Phase I (Fig. 7C), remaining nearly constant in Phase II; the average size of microlites decreases in Phase III. Plagioclase microlites of samples from the first stages of the eruption (EJ13A and EJ13B) also show the highest average aspect ratio (AR_{pl} = major/minor axis; 6.7–6.9; Fig. 7D), recording the occurrence of acicular microlites, respect to the generally bladed-shaped crystals of the other samples (average AR_{pl} around 3.7).

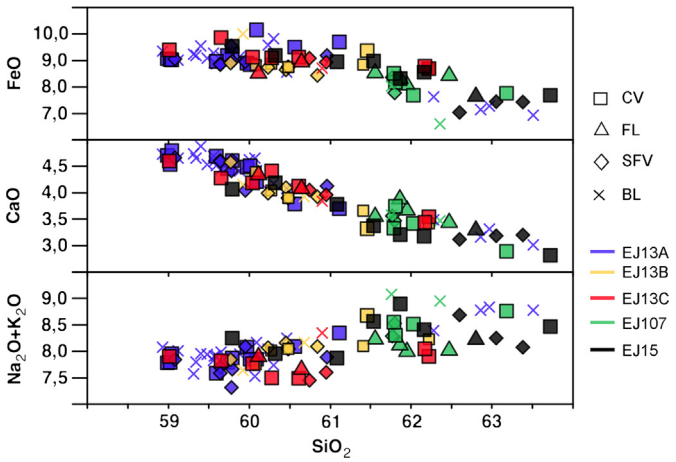

Fig. 8. Groundmass chemical analyses for the different samples (colored lines) and different clast types (different symbols). (For interpretation of the colours in this figure, the reader is referred to the web version of this article.)

4.3. Glass composition

Analyses of matrix glass were performed on the different types of ash fragments from all the studied samples, for a total of more than 100 clasts (Table 1, ESM). Glass composition ranges from benmoreite to trachyte (according to what observed by Gudmundsson et al., 2012) showing a rather wide variation in the silica content (56–68 wt%), with total alkali ranging from 7.3–9.1 wt%.

For CV, SFV and FL clasts no correlation is observed between groundmass glass composition, clast type and stratigraphic position of the sample (Fig. 8). BL clasts (mainly from EJ13A), span the same silica range covered by the other clast types and show slightly higher alkali content and lower MgO. Clasts from sample EJ13A have a wide variability, encompassing the whole compositional range. A shift toward more evolved compositions is shown by the average content of CaO and total alkalies (Fig. 8); in general, clasts from EJ13B and EJ13C are mainly benmoreitic, contrasting with clasts from EJ07, which are mostly trachytic (Table 1, ESM). Similarly to clasts from the first phase, those from EJ15 span a large compositional range, showing both trachytic and benmoreitic compositions. The occurrence of trachytic compositions in the clasts of Phase II contrasts with data of Gudmundsson et al. (2012), who report only benmoreitic compositions during this phase. We suggest that this discrepancy (although small, given that EJ07 sample lays just at the limit of the field benmoreite-trachyte) could be related to the small number of samples collected during this prolonged phase of the eruption, which could have been more complex than shown by Gudmundsson et al. (2012).

5. Discussion

Morphological, textural and compositional features of pyroclasts have often been used to discuss the relative roles of ascent-related magma degassing and magma/water interaction, as well as the influence of magma composition and rheology in generating many of the observed features of the clasts. Magmatic fragmentation of a melt rising into a conduit can be either related to brittle failure of the highly vesicular melt (by strain-induced, viscoelastic relaxation following rapid acceleration, or for sudden release of bubble overpressure) or to inertially driven ductile deformation caused by bubble growth during decoupled gas-melt ascent (Cashman et al., 2000). Namiki and Manga (2008) suggested that the viscosity limit for the passage from ductile to brittle fragmentation can be placed around 10^6 Pa s. On the other side, hydromagmatic fragmentation mainly derive from the different modalities of magma–water interaction (fuel–coolant interaction, bulk interaction steam explosivity, cooling-contraction granulation; Kokelaar, 1986; White et al., 2003). Many textural and morphological features are commonly considered as produced by magma–water interaction, like the presence of blocky, dense, poorly crystalline fragments in the deposits, the diffuse cracking by hydration or chilling on the external surface of the clasts, the heavy vesicle fillings or fine ash coatings on external surfaces (Heiken and Wohletz, 1985; Cioni et al., 1992; Dellino and La Volpe, 1996; Büttner et al., 1999). Conversely, in many hydromagmatic eruptions, magma–water interaction mainly induces changes in the dynamics of dispersal and deposition of the eruption products without influencing fragmentation at a large scale (Kokelaar, 1983; Barberi et al., 1989; Kokelaar, 1986; Cole et al., 2001).

Morphological and textural analyses of April–May 2010 Eyjafjallajökull ash evidence the presence of four main types of fragments, distributed with different proportions along the eruption sequence. In spite of these differences, clasts of variable type and from the same stratigraphic level share similar glass composition and groundmass crystallinity, excluding a dependence of the clast features on the chemical and mineralogical composition of the magma. Irrespective of the clast type, however, a compositional and textural trend is observed in the groundmass of the whole juvenile fraction, passing from the first to the last erupted products. All these data are discussed here in terms of the dynamics of eruption and fragmentation, degassing and crystallization of the magma, and of the distribution of physical and rheological properties inside the ascending magma column.

5.1. Fragmentation processes: the significance of the different types of juvenile clasts

Variations in the morphological features of the clasts can be interpreted in terms of the relative role played by different fragmentation processes during the eruption. The presence inside a single stratigraphic level of three to four different clast types suggests that fragmentation occurred over a heterogeneous magma column characterized by variable vesicularity and rheological features. The predominance of highly vesicular fragments in all the main phases of the eruption suggests a prominent and always active role of degassing-related magmatic fragmentation during the eruption. Estimates of dissolved water content in magma (Keiding and Sigmarsson, 2012) give values clustered around 1.3–1.4 wt%, up to a maximum of 1.8 wt%. In the assumption that H_2O was the main volatile phase in the magma, volatile saturation was reached at pressure around 20–30 MPa for conditions of equilibrium magma degassing. According to these calculations, degassing-driven magma fragmentation probably occurred in the last hundreds of meters of the conduit. Basing on the measured ranges of glass composition, vesicle and crystal content, and on the estimates of dissolved water content and magma temperature (around 1000 °C; Keiding and Sigmarsson, 2012), we calculate that magma (melt + crystals + bubbles) viscosity reached values at fragmentation of the order of 10^5–10^6 Pa s, close to the limit suggested by Namiki and Manga (2008) for the occurrence of ductile vs brittle fragmentation.

– BL clasts

BL clasts are abundant (40 vol.%) only in the sample of the onset of Phase I (Figs. 2, 3), where they are present as low crystallinity obsidian-like fragments with a fairly large range in vesicle shape (spherical to tubular) and abundance (12–40 vol.%). This type of particles was not described by other authors, who possibly failed to sample or did not analyze this thin proximal bed, representative of the first erupted products.

The textural features of BL clasts are important to define the role of hydromagmatic fragmentation in the eruption. We suggest that the glassy, dense BL clasts may represent fragments of the sill/dyke body intruded in the conduit and under an ice cover of about 200 m (Gudmundsson et al., 2012) during the initial phase of the eruption. The slow ascent of magma in the still cold host rocks and the intrusion at the base of the ice cover at the onset of the eruption favored processes of cooling and outgassing, with consequent delayed vesiculation followed by vesicle collapse; fragmentation of this part of the magma body was thus mainly related to interaction with ice, and was dominated by quenching granulation. Morphological features similar to those of BL clasts are described in effusive and effusive–explosive subglacial eruptions, as the product of the passive fragmentation of obsidian derived from the collapse of an erupting foam (Tuffen et al., 2002; Tuffen, 2007; Gudmundsson et al., 2012). These dense, microlite-poor clasts are completely lacking in the following activity, generally dominated by highly vesicular clasts, suggesting that water–ice access to the vent was very limited during late stages of the eruption. In addition, no other surface texture or morphology classically interpreted as derived from magma–water interaction (Heiken and Wohletz, 1985; Cioni et al., 1992; Büttner et al., 1999) was clearly observed in clasts from the other samples, reinforcing this conclusion.

A low amount of blocky clasts is also present in samples EJ13B to EJ15 (main stage of Phase I to Phase III); these clasts have an incipiently to poorly vesicular, microlite-rich groundmass, clearly contrasting with the glassy, nearly microlite-free nature of BL clasts observed in the first erupted products. Although not studied in detail here (for their low abundance), groundmass crystallinity of this second type of blocky clasts is generally higher even of all the other vesicular clasts present in the same samples. We suggest that these microlite-rich clasts derive from the shuttering of the syn-eruptively degassed, crystallized, more rigid (lateral?) portions of the magma column induced by the explosive fragmentation of the volatile-rich portions of the magma column.

– CV and SFV clasts

CV and SFV clasts are characterized by moderate to high vesicularity, and they dominate the entire sequence. They mainly differ in the range of size and aspect ratio of the vesicles. SFV have nearly equidimensional and homogeneously distributed vesicles, while in CV these are spherical to irregular with a larger dimensional range, possibly recording a more complex (and mature) vesiculation history (Fig. 5). On average, vesicles of SFV clasts differ from those of CV clasts for their unimodal distribution, smaller size and higher area number density (Figs. 5 and 6), suggestive of delayed nucleation. The external surface of the clasts cuts through a large amount of subspherical bubbles, suggesting they derive from the brittle, stress-dependent fragmentation of a magma column with a vertical and/or lateral gradient in vesicularity and cristallinity, well recorded in the gradually merging features of SFV and CV clasts. Textural features of SFV clasts of the samples from paroxysmal phases (EJ13B and EJ15; Phases I and III, respectively) differ from those of the milder Phase II (EJ07) or the end of Phase I (EJ13C). While during the high-intensity phases SFV clasts bear the smaller microlites, in samples from milder activity SFV clasts have the largest crystals (Fig. 7B and C). We suggest that SFV derive from the fragmentation of the deeper, volatile-rich part of the magma column, which is rapidly extracted and continuously renewed during the high mass discharge rate (MDR) phases, while during the lower intensity phases this part of the magma undergoes a slower ascent and minor undercooling. Similar gradual changes in groundmass texture observed on clasts from the summer 1980 pulsatory activity of Mt St Helens, were interpreted by Cashman and McConnell (2005) as related to the disruption of a vertically zoned magma column. Exsolution of magmatic volatiles and disintegration of the expanding, highly vesicular two-phase mixture were possibly the mechanisms that produced the SFV and CV fragments. The large abundance of these clasts (and in particular of SFV) in the deposits related to the events of higher intensity (Phases I and III) suggests that they were dominated by magmatic explosivity, and ash production was associated with stress-related, brittle disruption of a finely vesicular, foamy melt, in agreement with the interpretation of Dellino et al. (2012). The absence of a clear evidence (from clast morphology/surface texture) of hydromagmatic fragmentation suggests that, after the first most intense phase of the eruption, water access to the vent was limited, possibly due to the concurrent effects of the early formation of a large ice cauldron during the initial phase, efficient sub-glacier water drainage to feed jökulhlaups, and the progressive building, inside the ice cauldron, of a tephra edifice.

– FL clasts

FL clasts show the widest dimensional range of vesicles, due to the coexistence of large, irregular/elongated and small, nearly spherical vesicles (Fig. 5). The very smooth external surfaces and the generally contorted shapes (Fig. 3) represent the most remarkable feature of these clasts. Differently from the SFV clasts, FL clasts have morphological and textural features suggestive of the disruption of a heterogeneously vesicular fluid. The fluidal, contorted surfaces of the clasts possibly represent the internal walls of larger, elongated, coalescent vesicles broken at magma fragmentation. These bubbles record even more mature vesicularity than CV, and their elongated, aligned, contorted vesicles suggest at least partial development of vesicle connectivity and, possibly, of a higher permeability respect to SFV and CV clasts. The reaching of these conditions in the magma column by the end of Phase I and during Phase II (where FL clasts dominate) was related to the decrease in MDR, and could have caused the shift from stress-related, brittle fragmentation to dominant inertially-driven, ductile fragmentation (also in agreement with the proximity of magma viscosity to the threshold of ductile-brittle behavior).

5.2. Compositional and textural features of the ash as proxies for changes in magma dynamics

Important changes in the groundmass texture occur along the studied sequence and can be interpreted in terms of changes in the modalities of syn-eruptive magma ascent and decompression, and the contribution of different magma batches to the eruptive dynamics.

Conditions of fast magma ascent are recorded in the groundmass of clasts from the first stages of the eruption (EJ13A and EJ13B). In particular, these samples are characterized by the low groundmass crystal content and by the small size of the microlites; besides, plagioclase microlites are characterized by the high values of AR_{pl}. All these features are suggestive of large magma undercooling possibly related to rapid degassing under conditions of high volatile supersaturation (Cashman and Blundy, 2000; Hammer and Rutherford, 2002).

The increase of the average microlite size and the sharp drop in the value of AR_{pl} by the end of Phase I (from sample EJ13C to EJ15) mark the transition to Phase II, characterized by a general decrease in explosivity and the onset of the lava effusion. Interestingly, the groundmass glass of the Phase II clasts did not show the slight decrease in silica described by Gudmundsson et al. (2012), suggesting that the higher (and more variable) groundmass cristallinity of these products related to the decreased MDR and increased gas loss during this phase possibly contributed to buffer the residual melt on a trachytic composition.

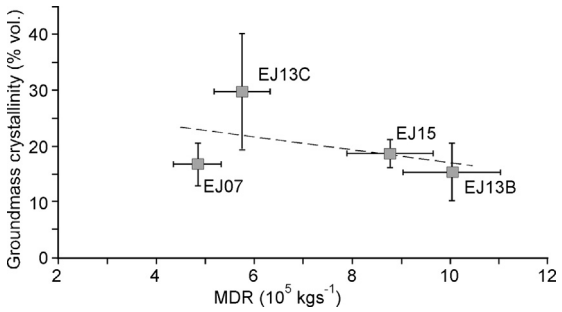

Fig. 9. Plot of the Mass Discharge Rate (MDR) vs groundmass crystallinity for the different samples (e.g. phases of the eruption).

An important change in the process of magma feeding is suggested to occur at the shift from Phase II to Phase III (5 May), when an arrival of primitive, deep-derived magma has been inferred mainly based on the presence of mafic minerals in disequilibrium with the evolved trachyandesite magma, accompanied by an increase in deep (18–23 km) seismicity (Sigmarsson et al., 2011; Tarasewicz et al., 2012). Sigmarsson et al. (2011) suggested that the arrival of this new, deeply derived magma contributed to remelt and remobilize a preexisting silicic intrusion, resulting in a small increase in silica of the erupting liquid clearly visible also in sample EJ15 (Fig. 8). Sigmundsson et al. (2010) suggested that the Phase III of the eruption was characterized by an increase in eruption rate with respect to Phase II, which coincided with a rapid increase in column height and with the concurrent cessation of lava effusion. The changes observed in the juvenile clasts, with an important decrease of FL type and the concurrent increase of SFV (Fig. 2), reflect this increase in explosivity. Vesicle number density returns close to the values of Phase I (Fig. 6), while the median vesicle size slightly increases with respect to the other samples. The lower number of FL clasts in Phase III testifies to a general decrease of large, interconnected bubbles in the magma column, in agreement with our hypothesis that the development of this type of vesicularity was mainly related to the decrease of MDR during Phase II, and the consequent trigger of a separated gas-melt dynamics. Also groundmass cristallinity gives indications similar to those for the first phase of the eruption (high undercooling, rapid magma ascent): the average size of microlites in the groundmass (both plagioclase and especially pyroxene; Fig. 7B, C) decreases with respect to the preceding phase, and the microlite number density increases. In general, microlite cristallinity roughly follows a trend of decrease with increasing magma discharge rate (Fig. 9), analogously to what observed by Wright et al. (2012) at Tungurahua. This suggests that rapid ascent of volatile-rich magma under nearly close degassing conditions was responsible of the episodes of higher explosivity of the eruption. Another important indication finally comes from the occurrence of microlite-rich blocky clasts, suggestive of the re-involvement, during the higher intensity Phase III, of partially degassed and crystallized portions of magma possibly left aside during the preceding, lower MDR Phase II.

5.3. A possible model for the eruption

All features of juvenile clasts well relate with observations of eruption dynamics, adding insights into the reconstructed model of the eruption (Gudmundsson et al., 2012). The opening stage of the summit eruption (first hours of Phase I, Fig. 10A) was characterized by magma intrusion into the glacier, and resulted in rapid magma quenching with the formation of microlite-poor obsidian and granulation by passive, not-explosive fragmentation. The simultaneous explosive activity was instead mainly driven by primary fragmentation of magma, as suggested by the concomitant presence of highly vesicular clasts (SFV and CV). Primarily fragmented magma possibly underwent a further stage of fragmentation by the contact with the ice-melting water.

The main stage of Phase I, characterized by the formation of an ash-laden plume and by hydromagmatic-style activity (Fig. 10B) immediately followed this subglacial activity (Gudmundsson et al., 2012). Tephra from this part of the eruption are characterized by a prevalent magmatic signature, with abundant, highly vesicular material (CV and SFV clasts). High magma ascent velocity during this high MDR phase favored conditions of closed-system degassing, which reflected in the generally low groundmass cristallinity (Figs. 7A and 9), the small average size of microlites (Fig. 7B and C) as well as the poorly connected vesicularity of CV and SFV clasts. Rapid ascent also resulted in brittle fragmentation of magma by development of vesicle overpressure. The interaction with ice–water which induced the observed hydromagmatic-style activity (cock-tail jets) occurred at the crater level with an already fragmented magma, strongly influencing the external dynamics of the eruption without an important contribution to the fragmentation process (Kokelaar, 1986). The final part of Phase I (sample EJ13C) was clearly characterized by a progressive decrease of eruptive intensity and by the building of an intracauldron cone, which insulated the magmatic mixture from the surrounding glacier. These conditions possibly promoted the passage to the mixed, effusive-explosive activity of Phase II (Fig. 10C), due to the possibility of creating a bifurcated conduit at the base of the tephra cone (Pioli et al., 2009). The decreasing MDR (Kaminski et al., 2011) induced also an increase of bubble interconnectivity (recorded in the mature vesicularity of CV and especially FL clasts) and the onset of separated gas-melt flow, resulting in a shift from stress-induced brittle magma fragmentation to dominant inertially-driven ductile fragmentation. The absence of evidences of magma–water interaction in the clast morphology suggests a prominent role of the growing tephra cone in preventing the free access of water to the vent (Tuffen et al., 2002; Tuffen, 2007).

Phase III (Fig. 10D) was characterized by the end of the effusive activity and by a rapid increase in eruption intensity. This higher-intensity phase was possibly related to the arrival of a new, gas-rich magma batch (Sigmarsson et al., 2011), as also suggested by the high, nearly spherical, small size vesicularity and the restoring of the closed-system conditions of degassing. Similarly to Phase II, water access to the vent area was limited to absent also during Phase III, resulting in the absence of the surtseyan-like explosivity at the vent typical of Phase I (Gudmundsson et al., 2012).

The abundant production of fine ash during the entire eruption is one of the main features of this event. Our data suggest that, despite the general interpretations of subglacial activity, magma–ice–water interaction played an important role in enhancing or promoting magma fragmentation only in the very initial phases of the activity, when the amount of available water was sufficiently high with respect to the erupting magma, and before the combined effects of the intracauldron tephra cone and water drainage from below the ice cap substantially inhibited the contact.

We suggest here that an additional process able to generate large amounts of ash was possibly related to the continuous recycling of large amounts of fragmented material accumulated in the ice cauldron. Comminution of this mixture by mechanical milling within the vent would be able to produce more fine ash from previously fragmented material (Rose and Durant, 2009). The pulsatory dynamics of the eruption, characterized by the high frequency emission of slowly rising ash-laden pulses that prematurely release a large mass of clasts over the vent area, supports this interpretation. The early settled material mixes with water inside the ice cauldron, forming a highly mobile tephra–water–ice slurry, prone to slide inside the vent and to be recycled by the sequence

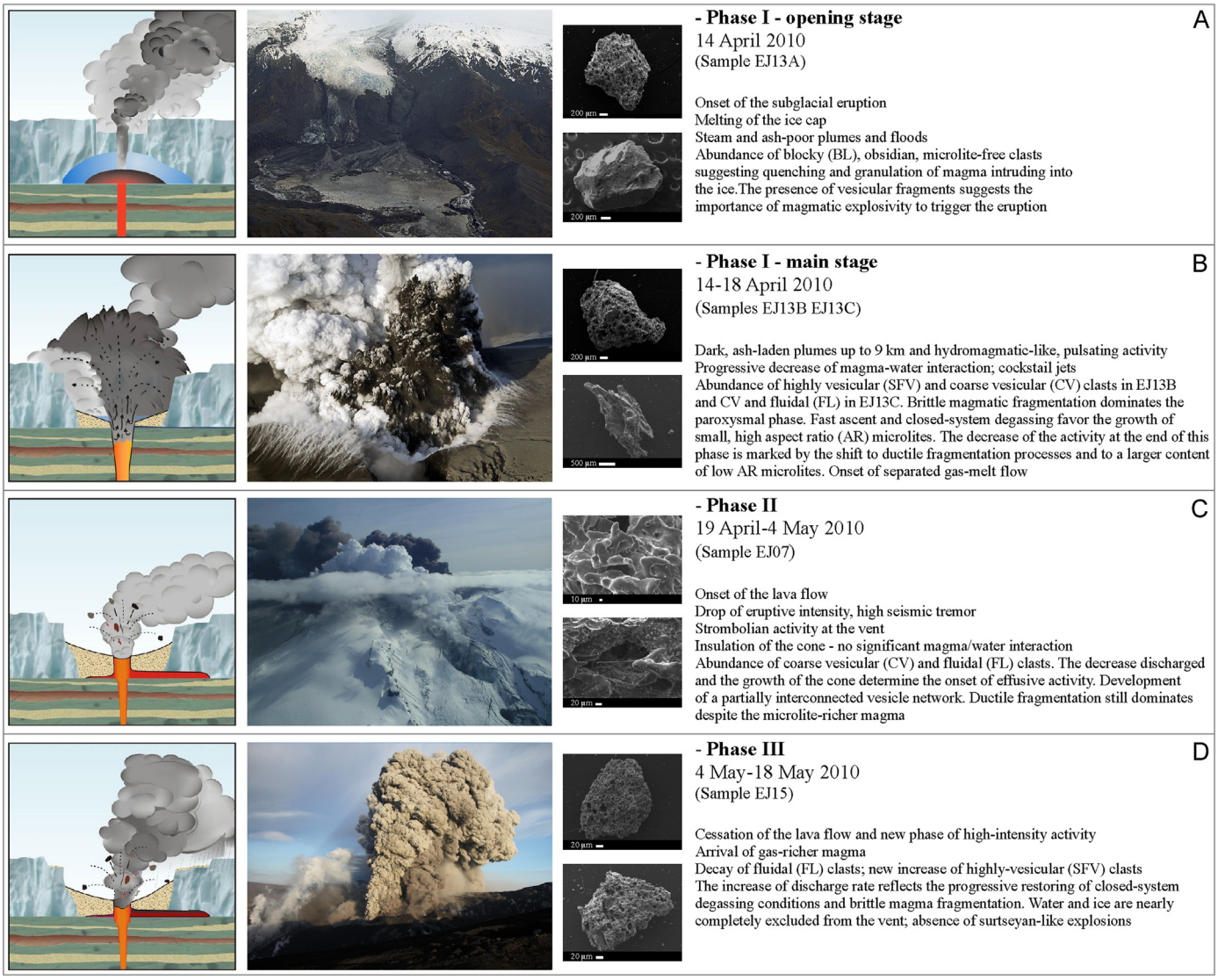

Fig. 10. Schematic representation of the different phases of the 2010 Eyjafjallajökull eruption. Pictures of Phase I are courtesy of M. Fulle – Stromboli Online (http://www.swisseduc.ch/stromboli/perm/iceland/index-it.html). Picture of Phase II is from F. Sigmundsson (http://www.jardvis.hi.is/Apps/WebObjects/HI.woa/wa/dp?id=1027696).

of explosive pulses. Further studies should be conducted to constrain the main parameters which control this process.

6. Conclusions

Some conclusions on the studied eruption and on the general problem of mid-intensity, ash dominated eruptions can be drawn from the presented results:

i. The presence of several types of juvenile clasts with different vesicularity and groundmass crystal content during each phase of the eruption suggests the fragmentation of a vertically heterogeneous magma column. The uneven distribution of gas vesicles within the magma column resulted in local conditions of closed and partially open degassing. A more efficient magma–gas decoupling established during the less intense phases of the eruption.

ii. The rheological properties of the magma, close to the threshold for the passage from ductile to brittle fragmentation, coupled with the variable MDRs (and hence magma ascent velocity) determined the conditions for the alternation among the two styles of magma fragmentation during the course of the eruption.

iii. The observed variation throughout the eruption of the magma composition possibly represents only a second order factor in producing important differences in morphology and texture of the ash fragments.

iv. The most evident feature of the summit eruption was clearly the production and dispersal of a large amount of fine ash. This has been traditionally interpreted as the result of an efficient magma–water (ice) interaction all along the eruption. Our data suggest that magma–water interaction was an efficient mechanism of fragmentation only during the very initial stage of the eruption, while primary magma fragmentation was always active throughout the eruption. Syn-eruptive clast recycling was possibly an additional mode of ash production, mainly related to mechanical milling in the vent structure.

v. The interaction of the erupting magma with ice and melting water mainly controlled the vent dynamics and the ash dispersal and deposition, driving early sedimentation of fine ash. The explosive activity which dominated the Phase I, reflects the presence of an important amount of ice-melt water into the eruptive vent, interacting with an already fragmented,

high-vesicularity magma, and can be explained by a process of bulk interaction steam explosivity (Kokelaar, 1986). The progressive formation of a tephra cone inside the ice cauldron possibly limited or completely excluded free access of melting water to the vent, and exerted an important control over the whole eruption dynamics, triggering the passage to effusive activity.

vi. All the above data suggest that caution should be used when assessing the role of magma–water interaction in dominating fragmentation processes in subglacial volcanism.

vii. The study demonstrates that detailed analysis of ash fragments is an important tool for understanding the dynamics of complex ash eruptions. In particular, we demonstrate that shape, composition, vesicularity and cristallinity of the ash well record the transitions in eruptive style and fragmentation dynamics that characterize these eruptions. Only few eruptions dominated by ash emission, up to now, have been studied with this detail, and our data, applied to a well known eruption like the Eyjafjallajökull 2010, are a clear demonstration of the potential of this method, which can help formulating conceptual models for this type of eruptions.

Acknowledgements

The authors are grateful to M. Rosi, M. Ripepe, R. Genco, D. Delle Donne, G. Lacanna, M. Hensch, and Þ. Sæmundsson for their contribution and discussion in the field. R. Cioni, M. Pistolesi and A. Bertagnini were supported by Italian Ministero Università e Ricerca funds, grant 20083MC8W2 (PRIN 2008–AshErupt project, responsible R. Cioni). C. Bonadonna was supported by a Fond National Suisse project (200020-125024). P. Pantani is acknowledged for graphical help during figure preparation. J. Gilbert, K. Cashman and an anonymous referee are deeply acknowledged for their constructive and sound comments on two different versions of this manuscript. We also want to acknowledge T. Elliott for his patience and availability to discuss all editorial requests and suggestions.

Appendix A. Supplementary material

Supplementary material related to this article can be found online at http://dx.doi.org/10.1016/j.epsl.2014.02.051.

References

Bagnato, E., Aiuppa, A., Bertagnini, A., Bonadonna, C., Cioni, R., Pistolesi, M., Pedone, M., Hoskuldsson, A., 2012. Scavenging of sulphur, halogens and trace metals by volcanic ash: the 2010 Eyjafjallajökull eruption. Geochim. Cosmochim. Acta 103, 138–160.

Barberi, F., Cioni, R., Rosi, M., Santacroce, R., Sbrana, A., Vecci, R., 1989. Magmatic and phreatomagmatic phases in explosive eruptions of Vesuvius as deduced by grain-size and component analysis of the pyroclastic deposits. J. Volcanol. Geotherm. Res. 38, 287–307.

Bonadonna, C., Genco, R., Gouhier, M., Pistolesi, M., Cioni, R., Alfano, F., Hoskuldsson, A., Ripepe, M., 2011. Tephra sedimentation during the 2010 Eyjafjallajokull eruption (Iceland) from deposit, radar, and satellite observations. J. Geophys. Res., Solid Earth 116.

Borisova, A.Y., Toutain, J.P., Stefansson, A., Gouy, S., de Parseval, P., 2012. Processes controlling the 2010 Eyjafjallajokull explosive eruption. J. Geophys. Res., Solid Earth 117.

Büttner, R., Dellino, P., Zimanowski, B., 1999. Identifying magma–water interaction from the surface features of ash particles. Nature 401, 688–690.

Cashman, K., Blundy, J., 2000. Degassing and crystallization of ascending andesite and dacite. Philos. Trans. R. Soc. Lond. A 358, 1487–1513.

Cashman, K.V., McConnell, S.M., 2005. Multiple levels of magma storage during the 1980 summer eruptions of Mount St. Helens, WA. Bull. Volcanol. 68, 57–75.

Cashman, K.V., Sturtevant, B., Papale, P., Navon, O., 2000. Magmatic fragmentation. In: Sigurdsson, H., Houghton, B.F., McNutt, S., Rhymer, H., Stix, J. (Eds.), Encyclopedia of Volcanology. Academic Press, San Diego, pp. 419–430.

Cioni, R., Sbrana, A., Vecci, R., 1992. Morphologic features of juvenile pyroclasts from magmatic and phreatomagmatic deposits of Vesuvius. J. Volcanol. Geotherm. Res. 51, 61–78.

Cioni, R., Sulpizio, R., Garruccio, N., 2003. Variability of the eruption dynamics during a Subplinian event: The Greenish Pumice eruption of Somma-Vesuvius (Italy). J. Volcanol. Geotherm. Res. 124, 89–114.

Cioni, R., Bertagnini, A., Santacroce, R., Andronico, D., 2008. Explosive activity and eruption scenarios at Somma-Vesuvius (Italy): Towards a new classification scheme. J. Volcanol. Geotherm. Res. 178, 331–346.

Cole, P.D., Guest, J.E., Duncan, A.M., Pacheco, J.M., 2001. Capelinhos 1957–1958, Faial, Azores: deposits formed by an emergent surtseyan eruption. Bull. Volcanol. 63, 204–220.

Dellino, P., La Volpe, L., 1996. Cluster analysis on ash particles morphology features to discriminate fragmentation dynamics in explosive eruptions. Acta Vulcanol. 8, 31–39.

Dellino, P., Gudmundsson, M.T., Larsen, G., Mele, D., Stevenson, J.A., Thordarson, T., Zimanowski, B., 2012. Ash from the Eyjafjallajokull eruption (Iceland): Fragmentation processes and aerodynamic behavior. J. Geophys. Res., Solid Earth 117.

D'Oriano, C., Bertagnini, A., Pompilio, M., 2011. Ash erupted during normal activity at Stromboli (Aeolian Islands, Italy) raises questions on how the feeding system works. Bull. Volcanol. 73, 471–477.

Gislason, S.R., Hassenkam, T., Nedel, S., Bovet, N., Eiriksdottir, E.S., Alfredsson, H.A., Hem, C.P., Balogh, Z.I., Dideriksen, K., Oskarsson, N., Sigfusson, B., Larsen, G., Stipp, S.L.S., 2011. Characterization of Eyjafjallajökull volcanic ash particles and a protocol for rapid risk assessment. In: Berner, Robert A. (Ed.), PNAS. Yale University, New Haven, CT. www.pnas.org/cgi/doi/10.1073/pnas.1015053108.

Gudmundsson, M.T., Thordarson, T., Hoskuldsson, A., Larsen, G., Bjornsson, H., Prata, F.J., Oddsson, B., Magnusson, E., Hognadottir, T., Petersen, G.N., Hayward, C.L., Stevenson, J.A., Jonsdottir, I., 2012. Ash generation and distribution from the April–May 2010 eruption of Eyjafjallajokull, Iceland. Sci. Rep. UK 2.

Hammer, J.E., Rutherford, M.J., 2002. An experimental study of the kinetics of decompression-induced crystallization in silicic melt. J. Geophys. Res., Solid Earth 107.

Hammer, J.E., Cashman, K.V., Voight, B., 2000. Magmatic processes revealed by textural and compositional trends in Merapi dome lavas. J. Volcanol. Geotherm. Res. 100, 165–192.

Heiken, G., Wohletz, K.H., 1985. Volcanic Ash. University of California Press, Berkeley. 245 pp.

Höskuldsson, Á., 2011. Eruption dynamics of the 2010 summit eruption at the Eyjafjallajökull volcano (Iceland): Magma fragmentation, tephra stratigraphy and transport. Geophys. Res. Abstr. 13, EGU2011-14165.

Kaminski, E., Tait, S., Ferrucci, F., Martet, M., Hirn, B., Husson, P., 2011. Estimation of ash injection in the atmosphere by basaltic volcanic plumes: The case of the Eyjafjallajokull 2010 eruption. J. Geophys. Res., Solid Earth 116.

Keiding, J.K., Sigmarsson, O., 2012. Geothermobarometry of the 2010 Eyjafjallajökull eruption. J. Geophys. Res. 117, B00C09. http://dx.doi.org/10.1029/2011JB008829.

Klug, C., Cashman, K.V., 1994. Vesiculation of May 18, 1980, Mount St. Helens magma. Geology 22, 468–472.

Kokelaar, B.P., 1983. The Mechanism of Surtseyan Volcanism. J. Geol. Soc. 140, 939–944.

Kokelaar, P., 1986. Magma–water interactions in subaqueous and emergent basaltic. Bull. Volcanol. 48, 275–289.

Lautze, N.C., Houghton, B.F., 2005. Physical mingling of magma and complex eruption dynamics in the shallow conduit at Stromboli volcano, Italy. Geology 33, 425–428.

Magnússon, E., Gudmundsson, M.T., Roberts, M.J., Sigurðsson, G., Höskuldsson, F., Oddsson, B., 2012. Ice–volcano interactions during the 2010 Eyjafjallajökull eruption, as revealed by airborne imaging radar. J. Geophys. Res. 117 (B7), B07405.

Miller, S.A., 2011. April 2010 UK Airspace closure: Experience and impact on the UK's air-travelling public and implications for future travel. J. Air Transp. Manag. 17, 296–301.

Nakada, S., Motomura, Y., 1999. Petrology of the 1991–1995 eruption at Unzen: effusion pulsation and groundmass crystallization. J. Volcanol. Geotherm. Res. 89, 173–196.

Namiki, A., Manga, M., 2008. Transition between fragmentation and permeable outgassing of low viscosity magmas. J. Volcanol. Geotherm. Res. 169, 48–60.

O'Regan, M., 2011. On the Edge of Chaos: European Aviation and Disrupted Mobilities. Mobilities 6, 21–30.

Pioli, L., Azzopardi, B.J., Cashman, K.V., 2009. Controls on the explosivity of scoria cone eruptions: Magma segregation at conduit junctions. J. Volcanol. Geotherm. Res. 186, 407–415.

Ripepe, M., Bonadonna, C., Folch, A., Delle Donne, D., Lacanna, G., Marchetti, E., Hoskuldsson, A., 2013. Ash-plume dynamics and eruption source parameters by infrasound and thermal imagery. The 2010 Eyjafjallajajokull eruption. Earth Planet. Sci. Lett. 366, 112–121.

Rose, W.I., Durant, A.J., 2009. Fine ash content of explosive eruptions. J. Volcanol. Geotherm. Res. 186, 32–39.

Self, S., Sparks, R.S.J., 1978. Characteristics of widespread pyroclastic deposits formed by the interaction of silicic magma and water. Bull. Volcanol. 41 (3), 196–212.

Sigmarsson, O., Vlastelic, I., Andreasen, R., Bindeman, I., Devidal, J.-L., Moune, S., Keiding, J.K., Larsen, G., Höskuldsson, A., Thordarson, Th., 2011. Remobilization of silicic intrusion by mafic magmas during the 2010 Eyjafjallajökull eruption. Solid Earth 2, 271–281.

Sigmundsson, F., Hreinsdóttir, S., Hooper, A., Árnadótir, T., Pedersen, R., Roberts, M.J., Óskarsson, N., Auriac, A., Decriem, J., Einarsson, P., Geirsson, H., Hensch, M., Ófeigsson, B.G., Sturkell, E., Sveinbjörnsson, H., Feigl, K.L., 2010. Intrusion triggering of the 2010 Eyjafjallajökull explosive eruption. Nature 468, 426–432. http://dx.doi.org/10.1038/nature09558.

Sparks, R.S.J., Bursik, M.I., Carey, S.N., Gilbert, J.S., Glaze, L.S., Sigurdsson, H., Woods, A.W., 1997. Volcanic Plumes. J. Wiley and Sons, Chichester, UK. 574 pp.

Taddeucci, J., Pompilio, M., Scarlato, P., 2004. Conduit processes during the July–August 2001 explosive activity of Mt. Etna (Italy): inferences from glass chemistry and crystal size distribution of ash particles. J. Volcanol. Geotherm. Res. 137, 33–54.

Taddeucci, J., Scarlato, P., Montanaro, C., Cimarelli, C., Del Bello, E., Freda, C., Andronico, D., Gudmundsson, M.T., Dingwell, D.B., 2011. Aggregation-dominated ash settling from the Eyjafjallajokull volcanic cloud illuminated by field and laboratory high-speed imaging. Geology 39, 891–894.

Tarasewicz, J., Brandsdottir, B., White, R.S., Hensch, M., Thorbjarnardottir, B., 2012. Using microearthquakes to track repeated magma intrusions beneath the Eyjafjallajkull stratovolcano, Iceland. J. Geophys. Res., Solid Earth 117.

Thordarson, T., 2010. The 2010 Eyjafoll eruptions, south Iceland: on-site observations and first analytical results. Geophys. Res. Abstr. 12, 15729.

Thorkelsson, B. (Ed.), 2012. The 2010 Eyjafjallajökull eruption, Iceland. Report to ICAO. http://www.vedur.is/media/ICAOreport_web.pdf.

Tuffen, H., 2007. Models of ice melting and edifice growth at the onset of subglacial basaltic eruptions. J. Geophys. Res., Solid Earth 112.

Tuffen, H., McGarvie, D.W., Gilbert, J.S., Pinkerton, H., 2002. Physical volcanology of a subglacial-to-emergent rhyolitic tuya at Raudufossafjöll, Torfajökull, Iceland. Geol. Soc. (Lond.) Spec. Publ. 202, 213–236.

White, J.D.L., Smellie, J.L., Clague, D.A., 2003. A deductive outline and topical overview of subaqueous explosive volcanism. In: White, J.D.L., Smelie JL Clague, D.A. (Eds.), Explosive Subaqueous Volcanism. In: AGU Geophysical Monograph, vol. 140, pp. 1–23.

Wright, H.M.N., Cashman, K.V., Mothes, P.A., Hall, M.L., Ruiz, A.G., Le Pennec, J.L., 2012. Estimating rates of decompression from textures of erupted ash particles produced by 1999–2006 eruptions of Tungurahua volcano, Ecuador. Geology 40, 619–622.

Zimanowski, B., Wohletz, K., Dellino, P., Büttner, R., 2003. The volcanic ash problem. J. Volcanol. Geotherm. Res. 122, 1–5.